NON-HYDROSTATIC ADIABATIC KERNEL FOR HIRLAM
Part III
Semi–implicit Eulerian scheme

Rein Rõõm, Aarne Männik
Tartu University, Estonia
Rein.Room@ut.ee, Aarne.Mannik@ut.ee

1 Introduction

In this paper, the adiabatic kernel of the nonhydrostatic HIRLAM with the semi-implicit Eulerian integration scheme is presented. The present investigation continues the work, initiated in the *Part I* by Rõõm (2001) and *Part II* by Männik and Rõõm (2001), where the fundamentals of nonhydrostatic atmospheric dynamics in pressure–related coordinates were presented, and on that basis, the nonhydrostatic, explicit-Eulerian version of HIRLAM was developed.

The new development supplements the nonhydrostatic Eulerian scheme with a semi-implicit integration option. In this respect, the new model represents a nonhydrostatic extension of the hydrostatic semi-implicit Eulerian HIRLAM (Kállen, 1996). However, by ideology, the parent model is the explicit-Eulerian nonhydrostatic scheme with completely anelastic pressure-coordinate dynamics, developed in Part I and Part II.

The semi-implicit method of integration in atmospheric dynamics was proposed by Robert (1969). Soon this method became a general approach in most numerical models of large-scale atmospheric dynamics. It is also applied in the hydrostatic HIRLAM. As is well-known, the main advantage of the semi-implicit scheme is the enhancement of the computational efficiency

of the model via the enlargement of the time-step. This is achieved through the reduction of the speed of sound and buoyancy wave motions in the modeled atmosphere. In mathematical sense, the semi-implicit scheme makes the numerical algorithm unconditionally stable with respect to the fast linear wave sub-system.

In the anelastic approximation used in the explicit version of the nonhydrostatic HIRLAM, the sound waves are filtered prior to the discretization, and the time-step is limited by the fastest internal buoyancy waves with the phase speeds of 100 m/s approximately. Due to this, the time-step of the explicit model is relatively large (approximately 1 minute at 10 km resolution), and the further time-step enhancement by a semi-implicit scheme is not so dramatic as in an elastic model or in the hydrostatic HIRLAM (where the time-step increase due to transition from the explicit Eulerian to the semi-implicit Eulerian scheme is of the order of two magnitudes). However, approximately a doubling of the time-step is achieved at 10 to 5 km resolutions. It is essential to note that the time-step increase is achieved at no extra computational cost, as the semi-implicit extension uses, in essence, the same basic integration algorithm as the explicit nonhydrostatic scheme. Therefore, the semi-implicit scheme will give rise to the numerical efficiency in comparison with the explicit model, even when the anelastic approximation is used, and consequently, this scheme is worth developing.

In the first half of the paper (section 2 and 3), the theoretical foundation of the semi-implicit model on the base of anelastic hybrid-coordinate model is presented. In the second half, after a minor discussion of numerical implementation details, modeling results with both the artificial flows over a bell-shaped mountain and with the realistic initial and boundary data are presented (Section 4). The main quality benchmark is the coincidence with the modeling results from the explicit version. A central parameter of the nonhydrostatic semi-implicit scheme is the Brunt-Väisälä frequency N. One of the central issues, addressed in this paper, is the proper choice of this quantity.

2 Semi-implicit equations

2.1 Initial equations with explicit separation of linear and nonlinear parts

We proceed from the discrete equations of motion in section 5, Part II. The indexing $\{i, j, k\}$ will be omitted, where appropriate, and a short notation for vertical differentiation will be used

$$\delta_p a: \quad (\delta_p a)_{ijk+1/2} = \left(\frac{\Delta_\eta a}{\overline{\Delta_\eta p}^{\eta}}\right)_{ijk+1/2}; \qquad \delta_p^+ b: \quad (\delta_p^+ b)_{ijk} = \left(\frac{\Delta_\eta b}{\Delta_\eta p}\right)_{ijk} .$$

Time differencing is denoted as δ_t:

$$\delta_t u = \frac{u^{t+\Delta t} - u^{t-\Delta t}}{2\Delta t} .$$

After explicit separation of linear terms in the tendencies F_u, F_v, F_T, and F_ω, equations (5.1.14), (5.2.1) – (5.2.3), (5.3.3a), (5.1.17) can be presented in the form

$$\hat{\mathbf{G}}^{+} \cdot \mathbf{v} + \delta_p^+ \omega = 0 , \tag{2.1.1a}$$

$$\delta_t \mathbf{v} = -\hat{\mathbf{G}}(\phi + \overline{\varphi}^{\eta}) + \mathbf{f_v} , \tag{2.1.1b}$$

$$\delta_t \omega = -\left(\frac{p}{\overline{H}^{\eta}}\right)^2 \delta_p \phi + F_\omega , \tag{2.1.1c}$$

$$\delta_t T = S\overline{\omega}^{\eta} + f_T , \tag{2.1.1d}$$

$$\Delta_\eta \varphi = -\alpha RT , \quad \Delta_\eta \overline{\varphi}^{\eta} = -\overline{\alpha RT}^{\eta} , \tag{2.1.1e}$$

where, $\hat{\mathbf{G}}^{+}$ and $\hat{\mathbf{G}}$ are defined by formulae (5.1.12) and (5.1.13) in Part II, $\mathbf{f_v} = \{f_u,\ f_v\}$ and f_T represent the nonlinear parts of the momentum and temperature tendencies at time level t:

$$f_{ui+1/2jk} = \left[\frac{-1}{\overline{h_x}^{x}}\left(-\overline{Z\overline{h_x}^{y}V}^{xy} + \delta_x E + \frac{\overline{h_x m\dot{\eta}}^{x}\Delta_\eta u}{\overline{\Delta_\eta p}^{x}}^{\eta}\right) + P_u + K_u\right]_{i+1/2jk} \tag{2.1.2a}$$

$$f_{vij+1/2k} = \left[\frac{-1}{\overline{h_y}^{y}}\left(\overline{Z\overline{h_y}^{x}U}^{yx} + \delta_y E + \frac{\overline{h_y m\dot{\eta}}^{y}\Delta_\eta v}{\overline{\Delta_\eta p}^{y}}^{\eta}\right) + P_v + K_v\right]_{ij+1/2k} \tag{2.1.2b}$$

where U, V are defined by (5.1.6), and Z, E are defined by (5.2.6) and (5.2.7), and

$$f_T = F_T - S\overline{\omega}^{\eta} = -\hat{a}(T) + \frac{\overline{\omega}^{\eta}\overline{\Delta_\eta T}^{\eta}}{\Delta_\eta p} + P_T + K_T \ , \qquad (2.1.2c)$$

with $\hat{a}(T)$ defined by (5.2.10) and F_T by (5.2.9).

The vertical momentum forcing F_ω coincides with (5.3.3b), which is completely nonlinear (does not include any linear term). The stratification term S in the temperature equation is

$$S_{ijk} = \left(\frac{\varkappa\alpha T - \overline{\Delta_\eta T}^{\eta}}{\Delta_\eta p} \right)_{ijk} \ . \qquad (2.1.3)$$

2.2 Semi-implicit discrete equations

The semi-implicit form of equations follows, when in the equations of motion (2.1.1b) – (2.1.1d) linear terms, responsible for wave-like motion, are treated implicitly:

$$\hat{\mathbf{G}}(\phi + \overline{\varphi}^{\eta}) \to \hat{\mathbf{G}}(\overline{\phi}^{t} + \overline{\varphi}^{\eta t}) \ , \quad \left(\frac{p}{\overline{H}^{\eta}}\right)^2 \delta_p \phi \to \left(\frac{p}{\overline{H}^{\eta}}\right)^2 \delta_p \overline{\phi}^{t} \ , \quad S\overline{\omega}^{\eta} \to S\overline{\omega}^{\eta t}$$

where $\overline{a}^{t}$ means the temporal averaging of the field a in respect to the time level t:

$$\overline{a}^{t} = \frac{a^{t+\Delta t} + a^{t-\Delta t}}{2} \ , \qquad \text{where} \qquad \overline{a}^{t} \equiv a(t)$$

and the short notation is used for double averaging $\overline{a}^{\eta t} \equiv \overline{\overline{a}^{\eta}}^{t}$. However, the averaged field $\overline{\phi}^{t}$ is, like ϕ in the explicit scheme, a diagnostic field, which will be evaluated from an explicit equation (the elliptic equation, see further), and there is no need to find or operate with its explicit and implicit parts (ϕ^t and $\Delta_{tt}\phi$) separately. Therefore, without being ambiguous, we will use the following notation

$$\phi \equiv \overline{\phi}^{t} \ .$$

The semi-implicit form of equations (2.1.1a) – (2.1.1d) is then

$$\hat{\mathbf{G}}^{+} \cdot \mathbf{v}^{\mathbf{t}} + \delta_p^{+}\omega^t = 0 \ , \qquad (2.2.1a)$$

$$\delta_t \mathbf{v} = -\hat{\mathbf{G}}(\phi + \overline{\varphi}^{\eta t}) + \mathbf{f}_{\mathbf{v}} \ , \qquad (2.2.1b)$$

$$\delta_t\omega = -\left(\frac{p}{\overline{H}^{\eta}}\right)^2 \delta_p\phi + F_\omega \ , \qquad (2.2.1c)$$

$$\delta_t T = S\overline{\omega}^{\eta t} + f_T \ , \qquad (2.2.1d)$$

$$\Delta_\eta\varphi^t = -(\alpha RT)^t \ , \quad \Delta_\eta(\overline{\varphi}^{\eta})^t = -(\overline{\alpha RT}^{\eta})^t \ . \qquad (2.2.1e)$$

The nonlinear forcings $\mathbf{f_v}$, F_ω, f_T, as well as the coefficients H, S, and the pressure p in linear terms are treated explicitly, i.e., they are given at the time level t. Diagnostic relationships (2.2.1a), (2.2.1e) also are explicit equations. Applying to $\overline{\varphi}^{\eta t}$ in (2.2.1b) and $\overline{\omega}^{\eta t}$ in (2.2.1d) the following identity

$$\overline{X}^t = X^t + \Delta_{tt}X \ ,$$

where $\Delta_{tt}X$ is defined as

$$\Delta_{tt}X = \frac{1}{2}(X^{t+\Delta t} + X^{t-\Delta t}) - X^t \ ,$$

equations (2.2.1b) and (2.2.1d) can be presented as

$$\delta_t\mathbf{v} = -\hat{\mathbf{G}}\phi - \hat{\mathbf{G}}\overline{\Delta_{tt}\varphi}^{\eta} + \mathbf{F_v} \ , \qquad (2.2.1b')$$

$$\delta_t T = S\overline{\Delta_{tt}\omega}^{\eta} + F_T \ . \qquad (2.2.1d')$$

As the tendencies F in equations (2.2.1b'), (2.2.1c), and (2.2.1d') are evaluated at time t and coincide with those of the explicit Eulerian scheme (see formulae (5.2.4), (5.2.5), (5.2.8), and (5.3.3b)), the obtained system differs from the explicit scheme by the presence of terms with the second order differences $\Delta_{tt}\phi$ and $\Delta_{tt}\omega$.

As (2.2.1a) holds at every time-level, it yields derivative relationships

$$\hat{\mathbf{G}}^+ \cdot \overline{\mathbf{v}}^t + \delta_p^+\overline{\omega}^t = 0 \ , \qquad (2.2.1a')$$

$$\hat{\mathbf{G}}^+ \cdot \delta_t\mathbf{v} + \delta_p^+\delta_t\omega = 0 \ . \qquad (2.2.1a'')$$

3 Integration of the semi-implicit system

In this section, the elliptic equation for ϕ is derived. It is a generalization of the elliptic equation for ϕ^t of the explicit scheme.The equation includes an elliptic main part and a small perturbation term. When solved iteratively, the algorithm draws back to the explicit case with an exception that the horizontal Laplacian in the elliptic equation is increased by the factor $1 + \Delta t^2 N^2$, N being the Brunt-Väisälä frequency.

3.1 The elliptic equation for baric geopotential

Elimination of time differences in (2.2.1a") with the help of (2.2.1b') and (2.2.1c) yields equation

$$\hat{\mathbf{G}}^{+} \cdot \hat{\mathbf{G}} \left(\phi + \overline{\Delta_{tt}\varphi}^{\eta} \right) + \widehat{\mathbf{L}}\phi = A_{\phi} \ , \tag{3.1.1a}$$

where

$$\widehat{\mathbf{L}}\phi = \delta_p^{+} \left(\frac{p^2}{(\overline{H}^{\eta})^2} \delta_p \phi \right) \tag{3.1.1b}$$

and

$$A_{\phi} = (\hat{\mathbf{G}}^{+} \cdot \mathbf{F}_{\mathbf{v}}) + \delta_p^{+} F_{\omega} \ . \tag{3.1.1c}$$

The mass balance condition for ϕ (Part II, equation (5.3.5)) becomes

$$\widehat{B}(\phi + \overline{\Delta_{tt}\varphi}^{\eta}) = b \ , \tag{3.1.1d}$$

where $\widehat{B}$is given by (5.3.5a) and

$$b_{ij} = \sum_{k=1}^{Nlev} \left[\delta_x \left(\overline{h_y}^{x} \overline{\Delta_{\eta} p}^{x} \hat{F}_u \right) + \delta_y \left(\overline{h_x}^{y} \overline{\Delta_{\eta} p}^{y} \hat{F}_v \right) \right]_{ijk}$$

$$+ (h_x h_y)_{ij} \left[\frac{\partial^2 \overline{p}_0}{\partial t^2} + \nabla \cdot \left(\frac{\partial \overline{p}_0}{\partial t} \sum_{k=1}^{Nlev} (\Delta_{\eta} B)_k \mathbf{v}_k \right) \right]_{ij} \ . \tag{3.1.1e}$$

Note that the formula for b_{ij} is corrected here, it is different from the old formula (5.3.5b), which was erroneous[1].

Except the term with the second order difference $(\overline{\Delta_{tt}\varphi}^{\eta})$, equation (3.1.1a) coincides with elliptic equation (5.3.4c) of the explicit scheme. Due to this additional term, equation (3.1.1a) is not closed and it must be complemented with an additional relationship between $(\overline{\Delta_{tt}\varphi}^{\eta})$ and ϕ. To obtain such a relationship, we rewrite the omega and temperature equations (2.2.1c) and (2.2.1d') in the form

$$\Delta_{tt}\omega = -\Delta t \left(\frac{p}{\overline{H}^{\eta}} \right)^2 \delta_p \phi + \mu_{\omega} \ , \tag{3.1.2a}$$

[1]However, this difference has no significance in practice, as it is almost negligible in actual atmospheric conditions.

$$\Delta_{tt}T = \Delta t S\overline{\Delta_{tt}\omega}^{\eta} + \mu_T \ , \qquad (3.1.2b)$$

where

$$\mu_\omega = \Delta t F_\omega - \omega^t + \omega^{t-\Delta t} \ , \quad \mu_T = \Delta t F_T - T^t + T^{t-\Delta t} \ . \qquad (3.1.2c)$$

Elimination of ω in (3.1.2b) with the help of (3.1.2a) yields

$$\Delta_{tt}T = -\Delta t^2 S\overline{\left(\frac{p}{\overline{H}}\right)^2 \delta_p\phi}^{\eta} + \mu_T + \Delta t S\overline{\mu_\omega}^{\eta} \ . \qquad (3.1.2d)$$

Further, the integrated presentation for the thermic geopotential is needed. It proceeds from (2.1.1e) with the help of the boundary condition $\varphi_{ijNlev+1/2} = gh_{ij}$

$$\overline{\varphi}^{\eta}_{ijk} = gh_{ij} + [\hat{M}(\alpha RT)]_{ijk} \ , \qquad (3.1.3)$$

$$[\hat{M}(a)]_{ijk} = \sum_{k'=k+1}^{Nlev} a_{ijk'} + \frac{1}{2}a_{ijk} \ . \qquad (3.1.4)$$

Applying here the operator Δ_{tt}, assuming that α and R are (approximately) constant[2] , and using (3.1.2d), the wanted relationship results:

$$\overline{\Delta_{tt}\varphi}^{\eta} = -Q(\phi) + Q^0 \qquad (3.1.5a)$$

where

$$Q(\phi) = \Delta t^2 \hat{M}\left[\alpha RS\ \overline{\left(\frac{p}{\overline{H}^{\eta}}\right)^2 \delta_p\phi}^{\eta}\right], \qquad (3.1.5b)$$

$$Q^0 = \hat{M}\left[\alpha R\left(\mu_T + \Delta t S\overline{\mu_\omega}^{\eta}\right)\right] \ . \qquad (3.1.5c)$$

It is advantageous to modify the sum in the right hand side of (3.1.5b), using identity

$$[\hat{M}(a\overline{b}^{\eta})]_k = \sum_{k'=k+1}^{Nlev} (\overline{a}^{\eta}b)_{k'-1/2} + \frac{1}{2}a_{Nlev}b_{Nlev+1/2} - \frac{1}{4}a_k(\Delta_\eta b)_k \ .$$

[2]Actually, the weights of levels α_{ijk} depend on time via background surface pressure $\overline{p_s}$, and R is time dependent in the moist air. However, in the present case, these dependencies are marginal and can be omitted in the relationship (3.1.5a).

The result of the transformation is

$$\frac{1}{\Delta t^2}Q_k(\phi) = \sum_{k'=k+1}^{Nlev}(N^2\Delta_\eta\phi)_{k'-1/2} +$$

$$\frac{1}{2}(\alpha RS)_{Nlev}\left(\frac{p^2}{(\overline{H}^\eta)^2}\delta_p\phi\right)_{Nlev+1/2} - \frac{1}{4}\left[(\alpha RS)\Delta_\eta\left(\frac{p^2}{(\overline{H}^\eta)^2}\delta_p\phi\right)\right]_k \ , \quad (3.1.6a)$$

where N is a discrete presentation for the Brunt-Väisälä frequency

$$N^2_{k-1/2} = \left[\frac{\overline{\alpha RS}^\eta p^2}{(\overline{H}^\eta)^2\overline{\Delta_\eta p}^\eta}\right]_{k-1/2} \ . \quad (3.1.6b)$$

Omitting from (3.1.6a) the last two terms, which present, respectively, the first- and second-order small contributions to the sum, and using presentation

$$\sum_{k'=k+1}^{Nlev}(N^2\Delta_\eta\phi)_{k'-1/2} = N^2_{Nlev+1/2}\phi_{Nlev} - N^2_{k+1/2}\phi_k - \sum_{k'=k+1}^{Nlev}\phi_{k'}(\Delta_\eta N^2)_{k'} \ ,$$

the final presentation for Q_k follows:

$$Q_k(\phi) = \nu^2_{Nlev}\phi_{Nlev} - \nu^2_k\phi_k - \sum_{k'=k+1}^{Nlev}\phi_{k'}\Delta_\eta\nu^2_{k'-1/2} \ , \quad (3.1.7)$$

where the non-dimensional parameter ν is

$$\nu^2_{ijk} = \Delta t^2 N^2_{ijk+1/2} \ . \quad (3.1.8)$$

Using (3.1.5a) and (3.1.7), the term $\phi + \Delta_{tt}\overline{\varphi}^\eta$ can be presented as

$$\phi_k + \overline{\Delta_{tt}\varphi_k}^\eta = (1+\nu^2_k)\phi_k - \nu^2_{Nlev}\phi_{Nlev} + \sum_{k'=k+1}^{Nlev}\phi_{k'}\Delta_\eta\nu^2_{k'-1/2} + Q^0_k \ . \quad (3.1.9)$$

This is the desired relationship which closes the system (3.1.1).

Thus, in the case of semi-implicit model, the time-integration problem (i.e.., the one-step-forecast problem) draws, in essence, back to the solution of the baric geopotential ϕ from the elliptic problem described by equations (3.1.1a), (3.1.1d) and (3.1.9). The situation is rather analogous to the explicit case,

where it was necessary to solve an analogous elliptic problem for the explicit component of the baric geopotential ϕ^t. The most important quality of the presented semi-implicit model is that there is no need to solve the elliptic equation for the explicit and implicit components ϕ^t and $\Delta_{tt}\phi$ separately[3] , as it is sufficient to have the solution for the sum $\phi = \phi^t + \Delta_{tt}\phi$.

3.2 Solution of the elliptic equation

Equations (3.1.1a), (3.1.1d) are rather similar to the corresponding equations of the explicit model (Eq. (5.3.4) and (5.3.5) in Part II) and approach the explicit case in the limit $\Delta t \to 0$. It is advantageous then to reduce the solution algorithm to the corresponding scheme of the explicit model.

In the following, the constant Brunt-Väisälä frequency approximation

$$N_{ijk} \approx N^* = \text{const}, \qquad \nu_{ijk} = \nu = \Delta t N^* = \text{const} \tag{3.2.1}$$

is used in the solution of the elliptic equation. The reason is that when the vertical derivative $\partial N/\partial p$ is locally large, the iterative algorithm will not converge. The non-iterative algorithm would be computationally expensive. Meanwhile, it is not clear either, whether the non-iterative solution is stable. At the same time, the algorithm with the constant N is non-expensive, computationally stable, and, as it will be demonstrated later in numerical experiments, approximation (3.2.1) does not affect the solution's precision.

The use of simplified background state in the semi-implicit adjustment procedure is not a specific feature of the current algorithm, but a rather general property of all semi-implicit schemes, which deal with the regularization of the internal wave mode. The need to treat the reference state isothermally was first discussed by Simmons *et al* (1978). The isothermal background reference temperature (yielding, by the way, the constant Brunt-Väisälä frequency), is also implemented in the hydrostatic HIRLAM, both in the Eulerian and Semi-Lagrangian integration schemes (Källén, 1996).

For the constant N, (3.1.9) simplifies to

$$\phi_k + \overline{\Delta_{tt}\varphi_k}^{\eta} = (1+\nu^2)\phi_k - \nu^2\phi_{Nlev} + Q_k^0. \tag{3.2.2}$$

The inversion algorithm will use an orthogonal basis. In this case, it is obligatory to supplement the source function with a singular term $\gamma_{ij}\delta_{kNlev}$

[3]However, the derivation of such equations is possible and straightforward.

to satisfy condition (3.1.1d)[4]. It is also convenient to treat $\rho_{ij} = \nu^2 \phi_{ijNlev}$ as an additional variable. The elliptic problem (3.1.1) reads then (only the vertical index k is shown explicitly):

$$(1+\nu^2)(\hat{\mathbf{G}}^+ \cdot \hat{\mathbf{G}}\phi)_k + (\widehat{\mathbf{L}}\phi)_k = A_{\phi,k} - (\hat{\mathbf{G}}^+ \cdot \hat{\mathbf{G}}Q^0)_k + (\hat{\mathbf{G}}^+ \cdot \hat{\mathbf{G}})_k \rho + \gamma \delta_{kNlev} \ , \tag{3.2.3a}$$

where γ_{ij} and ρ_{ij} have to be specified from equations

$$\widehat{B}[(1+\nu^2)\phi - \rho] = b - \widehat{B}[Q^0] \ , \tag{3.2.3b}$$

$$\rho = \nu^2 \phi_{Nlev} \ . \tag{3.2.3c}$$

The obtained system is close to the explicit case. The two differences are, first, the additional constant multiplier $(1+\nu^2)$ in front of the 'horizontal' Laplacian $\hat{\mathbf{G}}^+ \cdot \hat{\mathbf{G}}$, and, secondly, the additional variable ρ and equation for it (3.2.3c). The solution algorithm of equations (3.2.3) is as follows.

• As the **first step**, all operators in (3.2.3) are presented as the sums of horizontally homogeneous main parts and non-homogeneous perturbations

$$\hat{\mathbf{G}}^+ \cdot \hat{\mathbf{G}} = (\mathcal{L}_x + \mathcal{L}_y) + [\hat{\mathbf{G}}^+ \cdot \hat{\mathbf{G}}]' \quad , \mathbf{L} = \mathcal{L}_\eta + \mathbf{L}' \ , \quad \widehat{B} = \widehat{B}^0 + \widehat{B}' \ , \tag{3.2.4}$$

Horizontal mean operators $\mathcal{L}_x$, $\mathcal{L}_y$, $\mathcal{L}_\eta$, and $\widehat{B}^0$ are defined in Part II (formulae (5.3.9b),(5.3.9c), (5.3.10b)).

Using separation (3.2.4), system (3.2.3) is replaced with the iterative set of equations

$$(1+\nu^2)(\mathcal{L}_x + \mathcal{L}_y)\phi_k^{(l)} + (\mathcal{L}_\eta \phi^{(l)})_k = A_k^{(l)} + (\mathcal{L}_x + \mathcal{L}_y)\rho^{(l)} + \gamma \delta_{kNlev} \tag{3.2.5a}$$

$$\widehat{B}^0[(1+\nu^2)\phi^{(l)} - \rho^{(l)}] = b^{(l)} \ , \tag{3.2.5b}$$

$$\rho^{(l)} = \nu^2 \phi_{Nlev}^{(l)} \ , \tag{3.2.5c}$$

where $\{\phi^{(l)},\ \rho^{(l)},\ \gamma^{(l)}\}$ represent the lth iteration to the exact solution $\{\phi,\ \rho,\ \gamma\}$ for iterated sources

$$A_k^{(l)} = A_{\phi,k} - (\hat{\mathbf{G}}^+ \cdot \hat{\mathbf{G}}Q^0)_k - \{[(1+\nu^2)(\hat{\mathbf{G}}^+ \cdot \hat{\mathbf{G}})' + \widehat{\mathbf{L}}']\phi^{(l-1)}\}_k + [\hat{\mathbf{G}}^+ \cdot \hat{\mathbf{G}}]'_k \rho^{(l-1)} \ , \tag{3.2.5d}$$

[4]It would also be necessary to introduce analogous singular sources on lateral boundaries while solving the elliptic equation with non-homogeneous lateral boundary conditions. However, as the consideration is restricted to the model with Davies' boundary relaxation zone, the solution will be sought with homogeneous boundary conditions, and the lateral singular sources will not appear.

$$b^{(l)} = b - \widehat{B}Q^0 - (1+\nu^2)\widehat{B}'\phi^{(l-1)} + \widehat{B}'\rho^{(l-1)} \ . \qquad (3.2.5e)$$

• As the **second step**, the equation (3.2.5a) is solved for $\phi^{(l)}$ and for the optional right hand side, using three-dimensional orthogonal basis $\{X_{iq}Y_{kr}E_{ls}\}$ (Part II, Appendix C), where X, Y and E represent the eigenvectors of the one-dimensional Laplacians $\mathcal{L}_x$, $\mathcal{L}_y$, and $\mathcal{L}_\eta$, with eigenvalues $-\lambda_q^x$, $-\lambda_r^y$, and $-\lambda_s^\eta$, respectively. For X and Y the normalized discrete cosine-Fourier bases are used with eigenvalues given in (C.1c) of Part II. For E, the eigenvector problem, given in(C.3) of Part II is solved numerically.

Using notation

$$\tilde{\phi}_{qrs} = \sum_{ijk} X_{qi}Y_{rj}E^{-1}_{sk}\phi^{(l)}_{ijk} \ , \quad \tilde{A}_{qrs} = \sum_{ijk} X_{qi}Y_{rj}E^{-1}_{sk}A^{(l)}_{ijk} \ ,$$

$$\tilde{\gamma}_{qr} = \sum_{ij} X_{qi}Y_{rj}\gamma^{(l)}_{ij} \ , \quad \tilde{\rho}_{qr} = \sum_{ij} X_{qi}Y_{rj}\rho^{(l)}_{ij} \quad \tilde{b}_{qr} = \sum_{ij} X_{qi}Y_{rj}b^{(l)}_{ij} \ .$$

$$c_s = \sum_k \langle \Delta p \rangle_k E_{ks} \ , \quad d_s = \sum_k E^{-1}_{sk} \ ,$$

the solution of (3.2.5a) in the basis is

$$\tilde{\phi}_{qrs} = \frac{(\lambda_q^x + \lambda_r^y)d_s\tilde{\rho}_{qr} - \tilde{\gamma}_{qr}E^{-1}_{sNlev} - \tilde{A}_{qrs}}{(1+\nu^2)(\lambda_q^x + \lambda_r^y) + \lambda_s^\eta} \ . \qquad (3.2.6)$$

• As the **third step**, the coefficients γ and ρ are specified. For this, the solution (3.2.6) is substituted into equations (3.2.5b) and (3.2.5c). As the result, a two-dimensional set of linear algebraic equations follows for each pair of coefficients $\tilde{\gamma}_{qr}$, $\tilde{\rho}_{qr}$ (repetitive indexes q, r are omitted everywhere)

$$m_{11}\tilde{\rho} + m_{12}\tilde{\gamma} = n_1 \ , \qquad (3.2.7a)$$

$$m_{21}\tilde{\rho} + m_{22}\tilde{\gamma} = n_2 \ , \qquad (3.2.7b)$$

where

$$m_{11} = (\lambda^x + \lambda^y)\sum_s \frac{c_s d_s}{(1+\nu^2)(\lambda^x + \lambda^y) + \lambda_s^\eta} - \frac{\langle p \rangle_{Nlev+1/2}}{(1+\nu^2)} \ , \qquad (3.2.8a)$$

$$m_{12} = -\sum_s \frac{c_s E^{-1}_{s,Nlev}}{(1+\nu^2)(\lambda^x + \lambda^y) + \lambda_s^\eta} \ , \qquad (3.2.8b)$$

$$m_{21} = 1 - \nu^2(\lambda^x + \lambda^y) \sum_s \frac{E_{Nlev,s} d_s}{(1+\nu^2)(\lambda^x + \lambda^y) + \lambda_s^\eta} \ , \qquad (3.2.8c)$$

$$m_{22} = \nu^2 \sum_s \frac{E_{Nlev,s} E^{-1}_{s,Nlev}}{(1+\nu^2)(\lambda^x + \lambda^y) + \lambda_s^\eta} \ , \qquad (3.2.8d)$$

$$n_1 = \sum_s \frac{c_s \tilde{A}_s}{(1+\nu^2)(\lambda^x + \lambda^y) + \lambda_s^\eta} - \frac{\tilde{b}}{(1+\nu^2)\langle h_x \rangle \langle h_y \rangle (\lambda^x + \lambda^y)} \ , \qquad (3.2.8e)$$

$$n_2 = -\nu^2 \sum_s \frac{E_{Nlev,s} \tilde{A}_s}{(1+\nu^2)(\lambda^x + \lambda^y) + \lambda_s^\eta} \ . \qquad (3.2.8f)$$

After (3.2.7) is solved, solutions $\tilde{\gamma}$, $\tilde{\rho}$ are replaced into (3.2.6) and the resulting iterative solution is summed up

$$\phi^{(l)}_{ijk} = \sum_{qrs} X_{iq} Y_{jr} E_{ks} \tilde{\phi}_{qrs} \ . \qquad (3.2.9)$$

4 Numerical tests

The nonhydrostatic semi-implicit scheme described in the previous sections is realized numerically as the extension of the explicit-Eulerian HIRLAM. The pre- and post-processing facilities are completely those of the hydrostatic HIRLAM, also the lateral boundary treatment is the same (Davies' boundary relaxation scheme). The numerical code includes all hydrostatic (Eulerian explicit, Eulerian semi-implicit, Lagrangian semi-implicit) and nonhydrostatic (explicit and semi-implicit Eulerian) sub-models as options which may be switched on/off. The numerical code has a parallel realization on the Linux-cluster (Tartu Observatory, Estonia) and on the Cray T3E (FMI).

In the following, some provisional results are presented, the purpose of which is to demonstrate the computational efficiency and precision characteristics of the model.

4.1 Flow over artificial orography

The first group of test experiments contains a high-resolution adiabatic simulations with artificial orography and an artificial initial state. For orography serves, as usual, the 'Witch of Agnesi'-type isolated hill provides the orography

$$h(x,y) = \frac{h_0}{[1+(x/a_x)^2+(y/a_y)^2]^s} \ , \tag{4.1}$$

where h_0 is the mountain height and $a_x,\ a_y$ are the half-widths of the hill along coordinate axes. We use $s = 1.5$ when examining flow over an isolated mountain and $s = 1$ when looking at one dimensional flow with $a_y = \infty$.

The initial state is characterized with the reference temperature $T_0(p)$, and wind U, which is initially taken a constant in x-direction and then transformed to the mass-balanced wind (see formulae (6.1.1) - (6.1.3) in Part II). The mean surface pressure field $\overline{p}_0$ is specified from orography $h(x,y)$, using the barometric formula and a small correction $\delta p_0(y) = -(\overline{p_0}/RT_0(\overline{p_0}))fUy$, changing linearly in y-direction, is added to it to balance the background Coriolis force fU . Boundary conditions are presented by the boundary fields, which coincide with the background fields: $u_b = U,\ v_b = 0\ ,\ T_b = T_0(p)$.

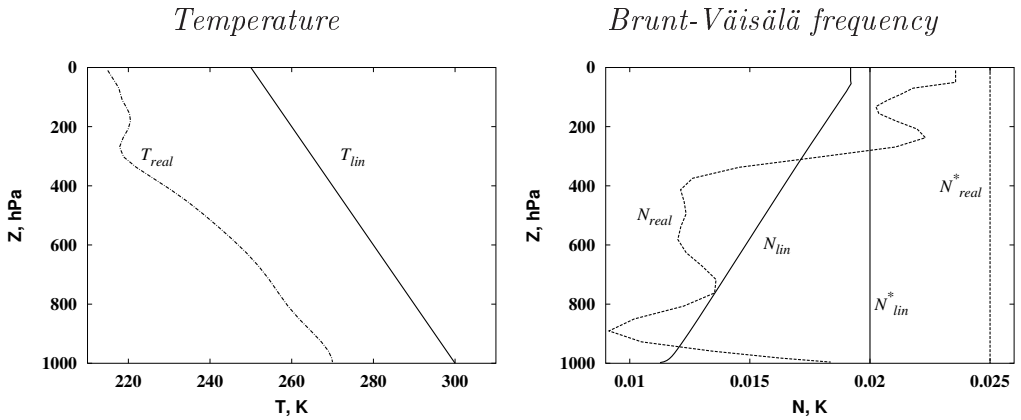

Fig. 1 *The temperature profiles and the corresponding Brunt-Väisälä frequencies used in the model experiments with artificial orography. The 'realistic' temperature distribution T_{real} corresponds to the mean (horizontally averaged) actual temperature distribution over Norway on March 21, 2001. N^*_{real} and N^*_{lin} are the constant values for the effective frequency N^* in the elliptic solver, corresponding to N_{real} and N_{lin}, respectively.*

The vertical resolution in the following tests is either 31 level (the standard case) or 60 level ECMWF η-levels.

The temperature profile is chosen differently in different experiments. The used temperature profiles $T_0(p)$ and the corresponding Brunt-Väisälä profiles $N(p)$ are shown in Fig. 1.

Effect of the time-step size on buoyancy waves

The first group of experiments is aimed at the study of the influence of time-step size on the buoyancy wave behavior. As is well-known, the excessively large time-step in the semi-implicit scheme causes systematic distortions of buoyancy waves (Haltiner and Williams 1980, Laprise and Peltier 1989).

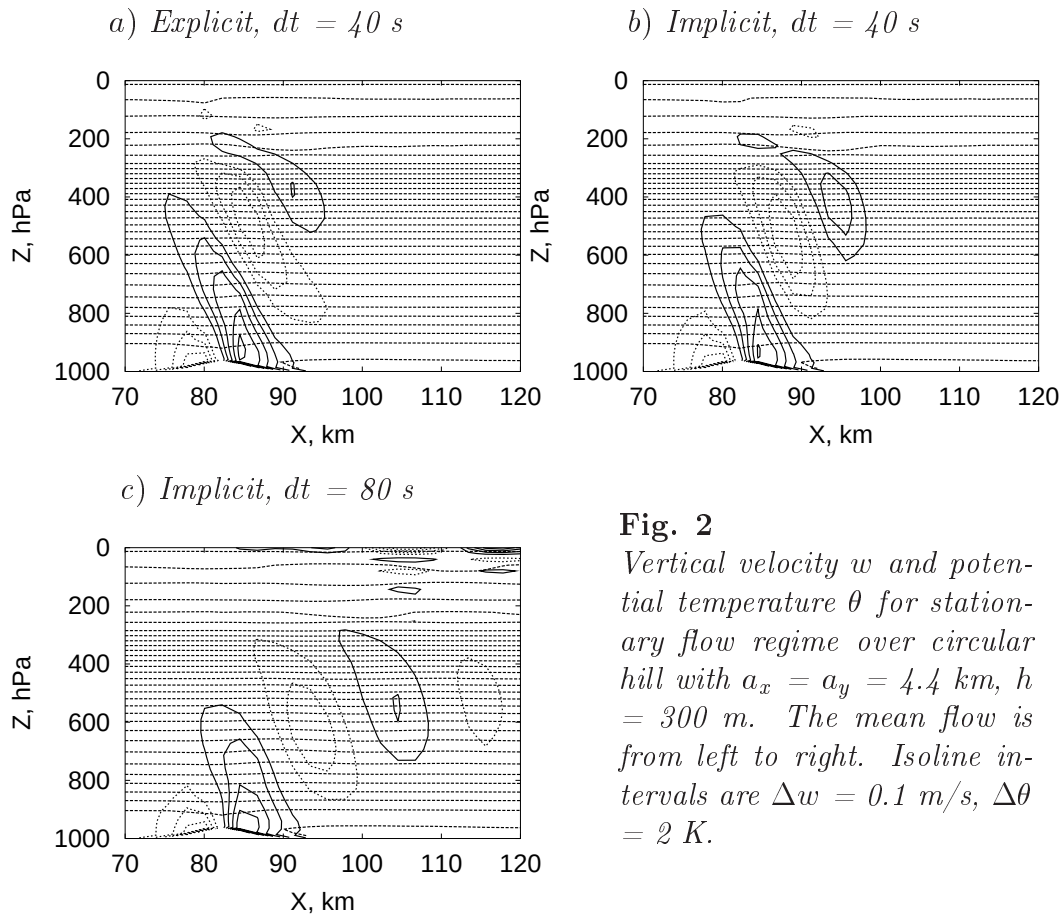

Fig. 2
Vertical velocity w and potential temperature θ for stationary flow regime over circular hill with $a_x = a_y = 4.4$ km, $h = 300$ m. The mean flow is from left to right. Isoline intervals are $\Delta w = 0.1$ m/s, $\Delta\theta = 2$ K.

As an example, the vertical velocity w and the potential temperature θ are shown in Fig. 2 for stationary flow over the circular hill with $a_x = a_y =$

4.4 km, $h = 300$ m. The temperature profile is T_{real} (see Fig. 1), and $U = 20$ m/s. In this experiment there are 114×100 grid-points with 2.2 km grid-step, and the vertical resolution is 31 levels. The explicit scheme with $dt = 40$ s (panel a), the semi-implicit scheme with the same time-step (panel b), and the semi-implicit scheme with $dt = 80$ s (panel c) are compared. This example shows the general feature of the semi-implicit integration: when the time-step is much larger than the maximum achievable time-step of the corresponding (acoustically filtered) explicit scheme, the modeled waves will have a strong spurious down-stream shift.

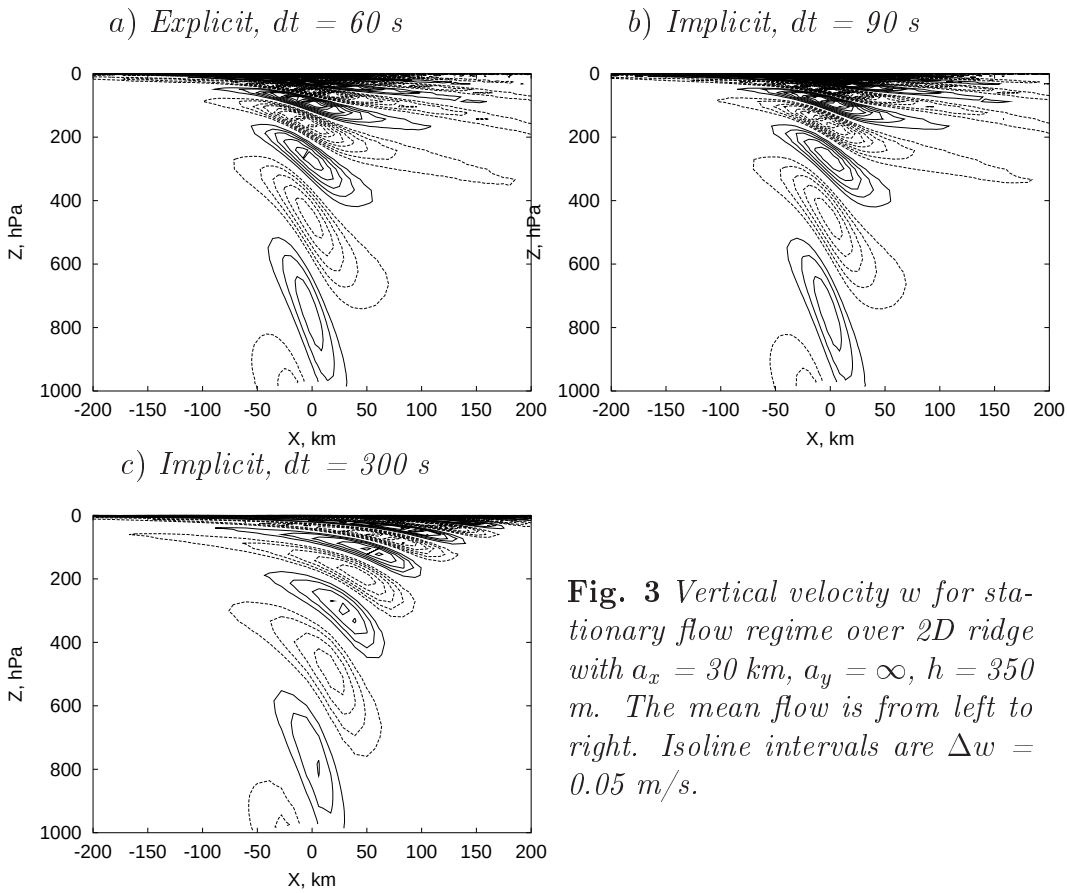

Fig. 3 *Vertical velocity w for stationary flow regime over 2D ridge with $a_x = 30$ km, $a_y = \infty$, $h = 350$ m. The mean flow is from left to right. Isoline intervals are $\Delta w = 0.05$ m/s.*

This is the consequence of the reduction of the buoyancy wave propagation speed by the implicit scheme, which results in the down-stream drift of stationary waves. A small distortion from the semi-implicit scheme is evident also at the moderate time-step, compare panel b with panel a in Fig. 2.

However, a strong distortion is seen for an 80 s time-step, see panel c of Fig. 2.

The down-stream drift is a physical effect in the case of short-scale orography, $a_x,\ a_y < 10$ km, as the buoyancy wave propagation speed is naturally small here. The problem is that for large time-steps the semi-implicit scheme reduces this speed even more, and makes the down-stream drift stronger than it actually should be. The false down-stream drift effect can become apparent already in the hydrostatic domain $a_x,\ a_y > 10km$, where the semi-implicit scheme, when used with a very large time-step, turns the flow apparently nonhydrostatic.

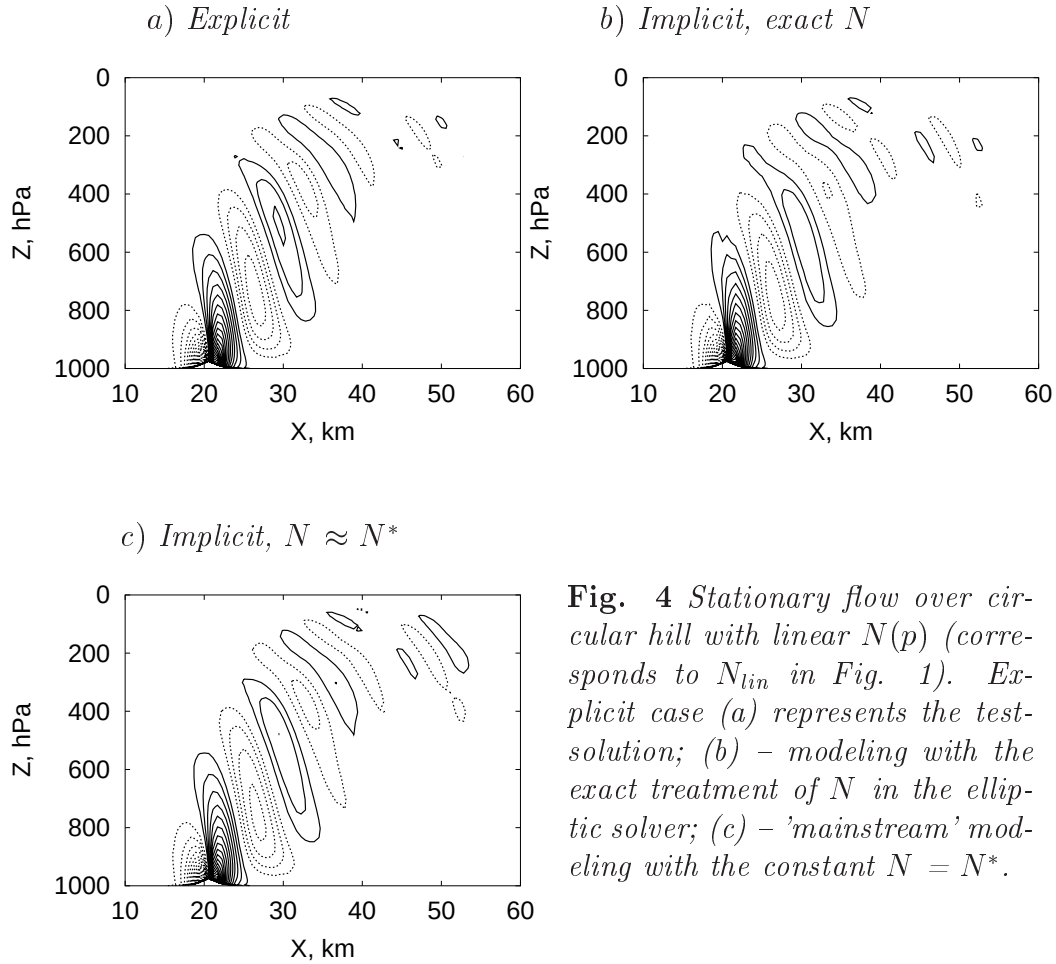

Fig. 4 *Stationary flow over circular hill with linear $N(p)$ (corresponds to N_{lin} in Fig. 1). Explicit case (a) represents the test-solution; (b) – modeling with the exact treatment of N in the elliptic solver; (c) – 'mainstream' modeling with the constant $N = N^*$.*

An example of such behavior is presented in Fig. 3 for a model flow with

$a_x = 30\ km$, $a_y = \infty$, $h_0 = 350\ m$, U = 30 m/s, $T_0 = 280\ K$ and $N = 0.018\ 1/s$ (isothermal atmosphere), grid 114×100, grid-step 11 km, 31 levels. As it can be seen, the use of the 5 minute time-step causes the systematic observable down-stream shift of the wave centers, which increases with the height. In addition, the wave pattern is systematically distorted. However, the distortions due to ultimately large time-steps are not so drastic, as they were for $a_x = 4.4$ km. For strong winds (50 - 70 m/s in the jet stream), the distorting effect becomes less, which is mainly the result of the comparatively small achievable time-step at these large material speeds. Another limiting case, where the distortions due to the large time-step have no effect, is the short-scale end of orography with a_x, $a_y \leq 0.5$ km, as here the time-step of the semi-implicit scheme will approximately coincide with the time-step of the explicit scheme (see further discussion).

Anyway, when attention is paid to the buoyancy waves, the time-step in the semi-implicit integration mode should not exceed too far over the maximum time-step of the (acoustically filtered) explicit one.

Effect of the Brunt-Väisälä frequency approximation

Another group of experiments with artificial flows was designed to study the influence of approximation $N(p) \to N^*$, (3.2.1), used in the elliptic solver. In the 'mainstream' algorithm, described in section 2.2, this approximation is used everywhere. The numerical values slightly exceeding the maximum of $N(p)$ are used for N^* (see Fig. 1). However, for checking whether the application of the actual $N(p)$ instead of the effective N^* would increase the model precision, a special modification of the semi-implicit scheme was modified to use $N(p)$ instead of constant N^*. In these experiments $N(p)$ was modeled with the $T_0(p)$, linear with the height (see T_{lin} in Fig. 1), to which corresponds an approximately linear profile of N (N_{lin}, *ibid*).

As an example, in Fig. 4, the results of the simulation of stationary flow over a 2D circular hill with $a_x = a_y = 1.5$ km, $h = 200$ m, $U = 20$ m/s, grid 114×100, grid-step 0.5 km, vertical resolution 60 levels are presented. The modeling result with the linear N (corresponding to N_{lin} in Fig. 1) is presented in panel b. It is compared to the explicit–mode integration (panel a) and to the 'mainstream' semi-implicit integration scheme, which makes use of the constant N^* (panel c).

As it can be seen from this comparison, the more detailed (exact in this particular case) treatment of N, instead of the constant-N-approximation,

actually does not add any refinement into the modeling results, but on the contrary, introduces some additional distortion.

Actually, there is no choice in the case of the real stratification (like N_{real} in Fig. 1), because the elliptic solver does not converge for the strong variability of the Brunt-Väisälä frequency. However, as the experience of modeling with the constant-N-approximation and comparison with the explicit scheme has shown, the constant-N-approximation enables reasonable accuracy along with the numerical stability.

4.2 Real data tests

In these experiments, the real observational initial and boundary data are used. The sub-grid physical parameterization is switched on, it represents the HIRLAM 5.0.0 standard physical package. In the implicit mode, the approximation of the constant Brunt-Väisälä frequency (3.2.1) is used in semi-implicit computations. Typically, for the effective Brunt-Väisälä frequency value $N^* = 1.2$ Max(N) is used.

Forecast experiment over flat region

Some examples of modeling with the new scheme are presented in Fig. 5a (surface pressure) and Fig. 5b (vertical cross-sections of wind and temperature fields). The 24h forecast on the 0.1 degree resolution, 114×100 point, 31 level grid is presented. Modeling area is the 'Estonian site', which represents a rather flat geographical region. The time steps in the explicit and semi-implicit nonhydrostatic schemes are 90 and 150 s, respectively. The figures demonstrate a very close coincidence of the semi-implicit and explicit nonhydrostatic algorithms. This is observable despite the large difference in the integration time-steps. The implicit scheme is not distorted by the excessively large time-step, which was observable in the experiments with an artificial isolated mountain and a uniform background stream. The absence of distorting effects in the case of the semi-implicit schemes can be explained with the small amplitude of buoyancy disturbances. Also, a close coincidence between the nonhydrostatic schemes and the semi-implicit hydrostatic model is observable, though the nonhydrostatic model gives a slightly deeper depression minimum in the center of the cyclone. In this example, the resolution belongs to the completely hydrostatic region, thus, there should be no significant differences between the hydrostatic and nonhydrostatic simulations, anyway.

Explicit non-hydrostatic

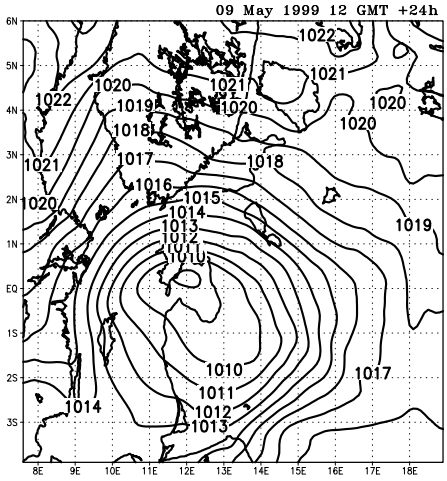

Semi-implicit non-hydrostatic

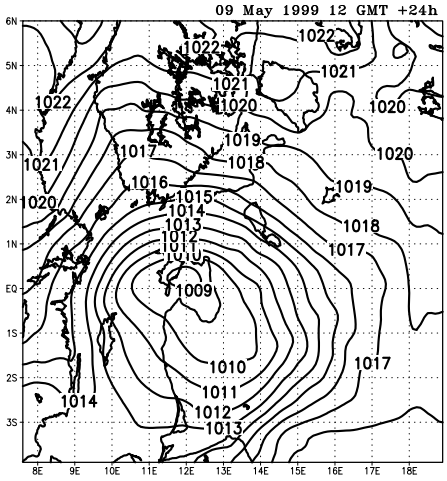

Hydrostatic

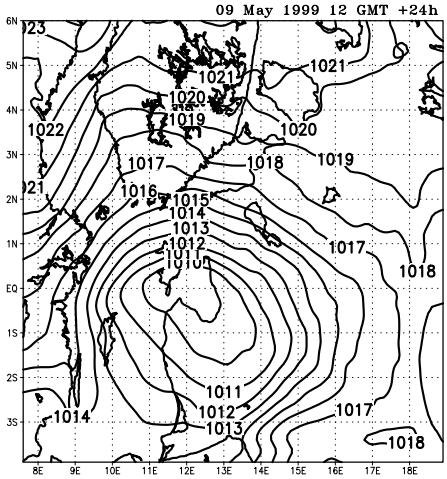

Fig. 5a *24h MSL pressure forecast with the explicit non-hydrostatic, semi-implicit non-hydrostatic, and semi-implicit hydrostatic schemes.*

Forecast experiment over mountainous region

An example of a 24 h forecast over Norwegian site with the nonhydrostatic semi-implicit, nonhydrostatic explicit, and hydrostatic models are presented in Fig. 6a (surface pressure), and Fig. 6b (vertical cross-sections of U-wind). Resolution is 0.05 degrees, grid size 156×156 points, vertical resolution is 31 levels. Time steps are 80 and 40 s, respectively. Despite of rather high orography, there is still a very close coincidence between the explicit and

semi-implicit nonhydrostatic schemes. This coincidence shows that the semi-implicit scheme produces adequate results.

Explicit non-hydrostatic

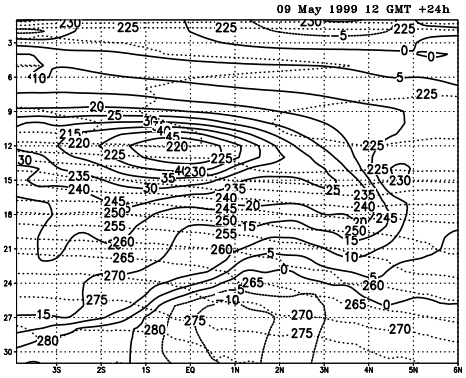

Semi-implicit non-hydrostatic

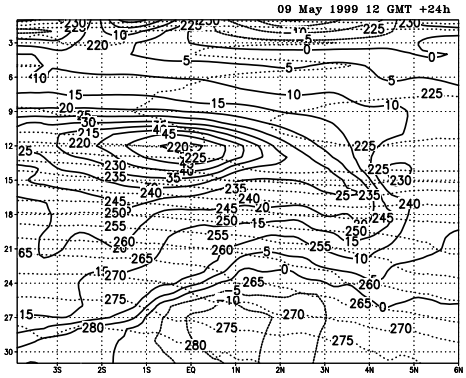

Hydrostatic

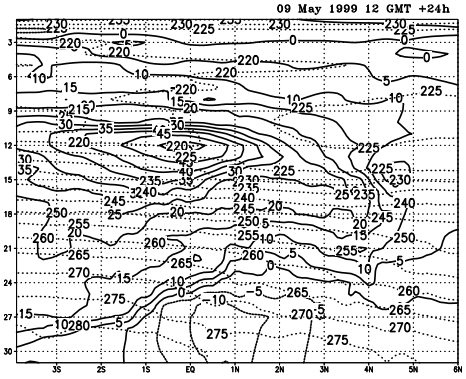

Fig. 5b *24h forecast for the vertical cross-sections (λ= 14E) of the U-wind and temperature with the explicit non-hydrostatic, semi-implicit non-hydrostatic, and semi-implicit hydrostatic schemes.*

The conclusion is that even in the case of high orography, the distorting mechanism due to a large time-step has no effect in real flow conditions. The lack of distortions can be explained by different factors, like the small amplitude of short-scale buoyancy waves, non-uniformity of wind, effects of sub-grid physics, or by the combination of all of these factors.

In this case, the nonhydrostatic simulation gives not large, but distinguishably different result from the hydrostatic model. In the large scale pattern, the predicted fields are rather similar. However, in fine details, the nonhydrostatic and hydrostatic models differ significantly. That means that the

nonhydrostatic effects can become evident at 5-km resolution, if the orography has a substantial height.

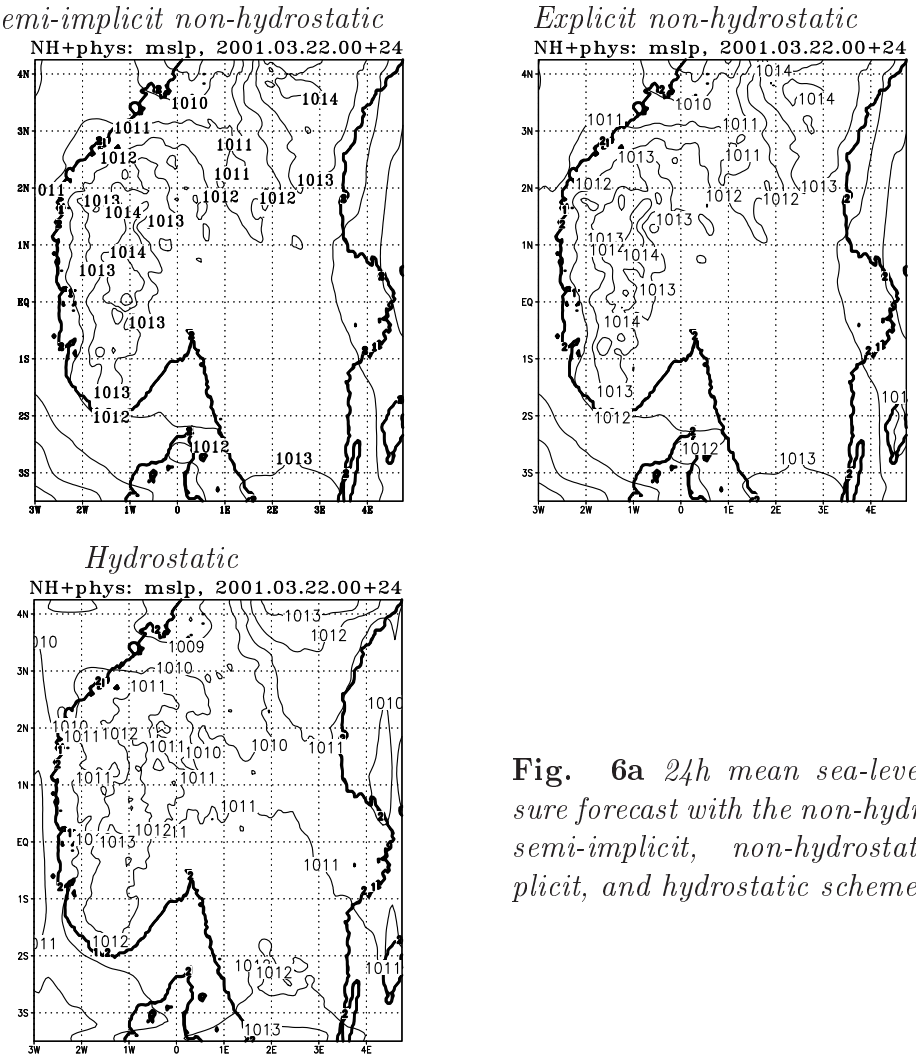

Fig. 6a *24h mean sea-level pressure forecast with the non-hydrostatic semi-implicit, non-hydrostatic explicit, and hydrostatic schemes.*

4.3 Computational efficiency

An essential benchmark of a numerical scheme is the achievable time-step, which is restricted by the Courant-Friedrichs-Lewy stability condition. Assuming that the flow is predominantly horizontal, this condition states for

explicit schemes

$$\Delta t < q\Delta X/max|\mathbf{v}+\mathbf{c}| \tag{4.2}$$

Semi-implicit non-hydrostatic

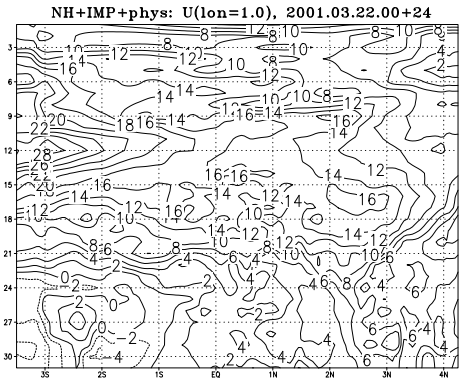

Explicit non-hydrostatic

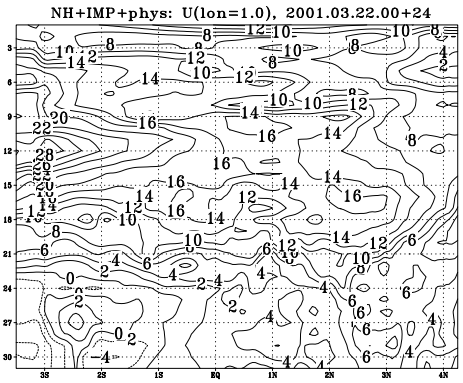

Hydrostatic

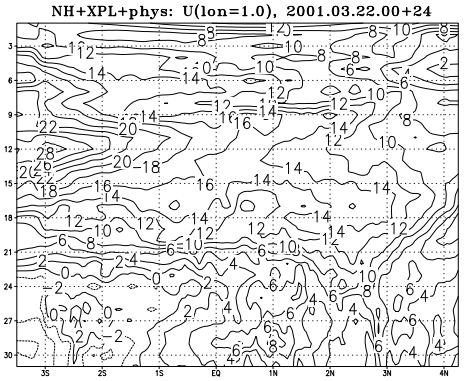

Fig. 6b *24h forecast for the vertical cross-sections (λ= 1E) of U-wind and temperature with the semi-implicit non-hydrostatic, explicit non-hydrostatic, and hydrostatic schemes.*

where ΔX is the horizontal grid step, $max|\mathbf{v}+\mathbf{c}|$ is the absolute maximum of the geometrical sum of material speed $\mathbf{v}$ and wave speed $\mathbf{c}$ in the medium, and the geometrical factor $q = 1$, and $q = 1/\sqrt{2}$, for one- and two-dimensional flows, respectively. In the acoustically non-adjusted case, $\mathbf{c}$ stands for the sound speed, and the maximum time-step is rather restricted. In the acoustically adjusted model, the acoustic mode is completely eliminated (including the external wave), and $\mathbf{c}$ represents the internal buoyancy wave speed. The speed of internal waves is dispersive and has a strong dependence on the dominant horizontal wave-length a, decreasing proportionally with a. In the case of orographically induced buoyancy waves, a is of the same order of the

horizontal scale of orography. Thus, shorter orography induces slower waves. As a result of the smaller wave speeds, the adjusted model supports much larger time-steps in comparison with the non-adjusted case.

In the semi-implicit scheme, the wave component is unconditionally stable, and the Courant-Friedrichs-Lewy condition applies to the material motion with the maximum velocity $max|\mathbf{v}|$:

$$\Delta t < q\Delta X/max|\mathbf{v}| \ . \tag{4.3}$$

Consequently, the semi-implicit model supports a larger time-step than the explicit one does. This advantage should be observable at long scales, when the activated internal buoyancy waves have long wavelengths, and should disappear at shorter scales.

In the Table 1, the maximum time-steps for the explicit and semi-implicit schemes are presented for flow over isolated mountain ridge ($a_y = \infty$ in (4.1) and $q = 1$ in (4.1) - (4.3)). The modeling is carried out for two background wind speeds, $U = 30\ m/s$, and $U = 100\ m/s$. As for a linear flow regime, modeled in these experiments, the velocity disturbance $\mathbf{v}' = \mathbf{v} - U\mathbf{i}$ is small and satisfies condition $max|\mathbf{v}'| << U$, the background value U can be approximately used for estimation of the maximum value $max|\mathbf{v}|$ in the Courant-Friedrichs-Lewy conditions (4.2) and (4.3).

TABLE 1

Maximum time-step Δt for explicit and semi-implicit schemes

ΔX	a_x	U	$\Delta X/U$	$\Delta t_{explicit}$	$\Delta t_{implicit}$
(km)	(km)	(m/s)	(s)	(s)	(s)
11	30	30	367	60	340
5.5	10	30	183	40	180
0.55	10	30	18.3	14	17
0.55	2.5	30	18.3	16	18
11	30	100	110	50	100
5.5	10	100	55	30	50
0.55	10	100	5.5	4	5
0.55	2.5	100	5.5	4	5

As expected, the semi-implicit scheme has the time-step close to the theoretical estimate $\Delta X/max(|\mathbf{v}|) \approx \Delta X/U|)$. Also it is seen that for $U = 30$ m/s, the semi-implicit scheme provides in comparison with the explicit adjusted case the time-step enlargement $340/60 \approx 5.7$ times at the 11 km resolution, and $180/40 = 4.5$ times at the 5.5 km resolution. For the strong wind $U = 100$ m/s, the gain in the time step is much modest. However, doubling at the 11 km resolution and enlargement by the factor $50/30 \approx 1.7$ at 5.5 km resolution is achieved. The case of the strong background wind $U = 100$ m/s is important for practical applications, as high wind speeds are often treated in the mighty jet-streams. As the figures of Table 1 demonstrate, approximate doubling at 11 km resolution and enlargement by the factor 1.7 at 5.5 km resolution is expected even in the most unfavorable conditions of a strong jet-stream.

At higher resolutions, where the speed of buoyancy waves decreases, the difference between the explicit and semi-implicit time-steps diminishes rapidly. At 0.55 km resolution, the difference is negligible for $U = 30$ m/s and constitutes about 1.2 times for $U = 100$ m/s.

The time-consumption rate (computation time per one time-step) of the semi-implicit model is slightly lower than in the explicit case. The integration algorithm in both schemes is basically the same, and this explains the similar time consumption rate. The slight additional economy in the semi-implicit case is achieved due to the smaller (in average over many time-steps) number of iterations at the solution of the elliptic problem (3.2.5), which, in its turn, is determined by the smoothing effect of the semi-implicit scheme (which is rather analogous to the smoothing effect of the spectral diffusion scheme).

5 Conclusions

The nonhydrostatic semi-implicit Eulerian version of the adiabatic kernel of HIRLAM has been presented in this paper. The model is a rather straightforward extension of the explicit Eulerian realization of anelastic pressure-coordinate dynamics. As the numerical tests show, the semi-implicit version maintains the precision characteristics of the explicit model, while giving rise to computational efficiency and numerical stability. The numerical efficiency depends on the model resolution and on the maximum wind speed. At 5 - 10 km horizontal resolutions, the model is at least 1.5 - 2 times more ef-

fective than its explicit, acoustically adjusted relative, but this advantage diminishes rapidly with shorter grid-steps and makes negligible at 0.5 km resolution. However, the larger stability advantage, which becomes evident via lesser spectral smoothing requirement, remains.

The model is implemented numerically in the parallel-computing HIRLAM environment. The numerical scheme is congruous with the remaining numerics of HIRLAM, and may be switched on as an option in the common hydrostatic HIRLAM.

Acknowledgments

This investigation has been supported by the **Estonian Science Foundation** under grant 4700.

R. Rõõm had support of the **Academy of Finland** (grant 51714).

A. Männik is supported by the **Väisälä Foundation** under the auspice of the **Finnish Academy of Sciences**.

6 References

Haltiner, G. J., and R. T. Williams 1980: *Numerical Prediction and Dynamic Meteorology.* John Wiley & Sons, New York, 477 p.

Källén, E. (Ed.), 1996: HIRLAM Documentation Manual, System 2.5. Norrköping, 262 pp.

Laprise, R. and W. R. Peltier, 1989: On the structural characteristics of steady finite-amplitude mountain waves over bell-shaped topography. *J. Atmos. Sci.*, **46**, 586 – 595.

Männik, A. and R. Rõõm, 2001: Non-hydrostatic adiabatic kernel for HIRLAM. Part II: Anelastic, hybrid-coordinate, explicit-Eulerian model. *HIRLAM Technical Report*, **49**, 54p.

Robert, A. J., 1969: The integration of a spectral model of the atmosphere by the implicit method. *Proc. WMO-IUGG Symposium on NWP*, Tokyo, Japan Meteorological Agency, VII, 19 - 24.

Rõõm, R., 2001: Nonhydrostatic adiabatic kernel for HIRLAM. Part I: Fundametals of nonhydrostatic dynamics in pressure-related coordinates. *HIRLAM Technical Report*, **48**, 26p.

Simmons, A. J., B. J. Hoskins and D. M. Burridge, 1978: Stability of the semi–implicit method of time integration. *Mon. Weather Rev.*, **106,** 405 – 412.